

A density-wave-like transition in the polycrystalline V_3Sb_2 sample with bilayer kagome lattice

N. N. Wang,^{1,2} Y. H. Gu,^{1,2} L. F. Shi,^{1,2} Q. Cui,^{1,2} K. Y. Chen,^{1,2} Y. X. Wang,^{1,2} H. Zhang,^{1,2} H. X. Yang,^{1,2} X. L. Dong,^{1,2} K. Jiang,^{1,2} J. P. Hu,^{1,2} B. S. Wang,^{1,2} J. P. Sun^{1,2} and J.-G. Cheng^{1,2*}

¹*Beijing National Laboratory for Condensed Matter Physics and Institute of Physics, Chinese Academy of Sciences, Beijing 100190, China*

²*School of Physical Sciences, University of Chinese Academy of Sciences, Beijing 100190, China*

*Email: jgcheng@iphy.ac.cn

Abstract

Recently, transition-metal-based kagome metals have aroused much research interest as a novel platform to explore exotic topological quantum phenomena. Here we report on the synthesis, structure, and physical properties of a bilayer kagome lattice compound V_3Sb_2 . The polycrystalline V_3Sb_2 samples were synthesized by conventional solid-state-reaction method in a sealed quartz tube at temperatures below 850 °C. Measurements of magnetic susceptibility and resistivity revealed consistently a density-wave-like transition at $T_{dw} \approx 160$ K with a large thermal hysteresis, even though some sample-dependent behaviors are observed presumably due to the different preparation conditions. This transition can be suppressed completely by applying hydrostatic pressures of about 1.8 GPa, but no sign of superconductivity is observed down to 1.5 K in the vicinity of putative quantum critical point of the density-wave order. The specific-heat measurements reveal a relatively large Sommerfeld coefficient $\gamma = 18.5$ mJ/mol-K², confirming the metallic ground state with moderate electronic correlations. Density functional theory calculations indicate that V_3Sb_2 shows a non-trivial topological crystalline property. Thus, our study makes V_3Sb_2 a new candidate of metallic kagome compound to study the interplay between density-wave-order, nontrivial band topology, and possible superconductivity.

Keywords: V_3Sb_2 , kagome metal, charge density wave, pressure effect

Introduction

The kagome lattice compounds consisting of corner-shared triangular network have been the focus of extensive investigations over last decades because they can host fascinating physical phenomena ranging from geometrically frustrated magnetism to nontrivial band topology [1-13]. When the localized moments are situated on the kagome lattice, frustrated spin interactions can lead to exotic magnetic ground states such as the quantum spin liquid state extensively studied in the herbertsmithite $\text{ZnCu}_3(\text{OH})_6\text{Cl}_2$ [14-19]. On the other hand, when the itinerant electrons are present, the metallic kagome lattice compounds hold the gene to achieve nontrivial electronic band structure containing Dirac cones, flat band, and van Hove singularities [20-24]. Upon proper electron filling, these features can promote novel correlated and/or topological states, such as bond density wave order [23,25], valence-bond state [26], chiral spin-density-wave (SDW) order [21], nontrivial charge-density-wave (CDW) order [1,27-29], and exotic superconductivity [12,23,30], etc. Thus, much recent experimental effort has been devoted to the metallic 3d transition-metal-based kagome systems.

For the correlated magnetic kagome metals, the coexistence of spin and charge degrees of freedom lead to the emergence of many novel quantum phenomena with nontrivial electronic behaviors. For example, large anomalous Hall effect (AHE) and Dirac fermions have been realized in the ferromagnetic Fe_3Sn_2 with flat-band dominated electronic band structure [7,31,32] and the quantum-limit Chern ferromagnet TbMn_6Sn_6 [13]. Large intrinsic AHE has been observed in ferromagnetic Weyl semimetal $\text{Co}_3\text{Sn}_2\text{S}_2$ [6,33] and noncollinear antiferromagnetic Mn_3Sn [34]. Dirac fermions has also been revealed in the antiferromagnetic FeSn [10,35]. For the recently discovered AV_3Sb_5 ($A = \text{K}, \text{Rb}, \text{Cs}$) family with quasi-2D ideal kagome layers of V ions, no static magnetic order was observed but they exhibit the coexistence and complex competition between superconductivity and chiral CDW in addition to giant AHE and pair density wave state [12,27-29,36-49]. For this latter class of materials, there are still many open issues, such as the nature of superconductivity and the mechanism of chiral CDW order.

Since the materials' realizations are scarce, it is indispensable to find more metallic kagome lattice compounds. To this end, we focus our attention on a simple binary compound V_3Sb_2 , which is isostructural to Fe_3Sn_2 and contains bilayer kagome lattice of V ions [31]. This material has been known to exist at temperatures below 875 ± 25 °C in the V-Sb phase diagram [50], but its physical properties have not been studied in detail to the best of our knowledge. In this work, we successfully synthesized nearly pure V_3Sb_2 polycrystalline sample and then characterized its structure, electrical transport, magnetic and thermodynamics properties at ambient or high pressures. Our results reveal a density-wave-like transition at $T_{\text{dw}} \approx 160$ K, which is evidenced by a clear anomaly in both magnetic susceptibility and resistivity. This compound shows no long-range magnetic order and superconductivity down to 1.5 K even after the density-

wave-like transition being suppressed completely by hydrostatic pressures. Since our density functional theory calculations show that V_3Sb_2 has a non-trivial topological crystalline property, the present study indicates that it may serve as a new metallic Kagome system to study the interplay between density-wave-order, nontrivial band topology and possible superconductivity.

Experimental and calculation details

Polycrystalline samples of V_3Sb_2 were synthesized by the traditional solid-state-reaction method. V powder (99.99 %) and Sb powder (99.99 %) in the molar ratio 3:2 were thoroughly mixed and pressed into a pellet, which was then placed into a quartz tube and sealed under high vacuum ($\sim 5 \times 10^{-4}$ Pa). The sealed ampoule was slowly heated to 700 °C and held for 48 hours, and then sintered again at 750-850 °C for 48 hours several times with intermediate grinding and pelletizing. According to the V-Sb phase diagram, the LT-phase of V_3Sb_2 with the Fe_3Sn_2 -type structure is stable below the peritectoid temperature of 875 ± 25 °C, above which the V-deficient $V_{2-x}Sb$ phase is more stable [50]. Phase purity of the obtained V_3Sb_2 polycrystalline samples was examined by powder X-ray diffraction (XRD) at room temperature with a $Cu-K\alpha$ radiation. In order to extract structural parameters, the refinements of the crystal structure were performed by the Rietveld method, using the FULLPROF program. The magnetic properties were measured with a Quantum Design Magnetic Property Measurement System (MPMS-III). Heat capacity and electrical transport measurements were carried out by using a Quantum Design Physical Property Measurement System (PPMS, 14 T). High-pressure resistivity was measured by using a self-clamped piston-cylinder cell under various hydrostatic pressures up to 1.81 GPa [51]. Daphne 7373 was used as the pressure transmitting medium and the pressure values were determined from the relative shift of the superconducting transition temperature of Pb.

Our density functional theory (DFT) calculation employs the Vienna ab initio simulation package (VASP) code [52] with the projector augmented wave (PAW) method [53]. The Perdew-Burke-Ernzerhof (PBE) [54] exchange-correlation functional is used in our calculations. The kinetic energy cutoff is set to be 600 eV for the expanding the wave functions into a plane-wave basis in VASP calculations while the energy convergence criterion is 10^{-6} eV. The Γ -centered k-mesh is $8 \times 8 \times 8$. The spin-orbital coupling is included in our DFT calculation. The calculation of topological indices employs vasp2trace program on Bilbao Crystallographic Server [55-57].

Results and Discussion

We have attempted to prepare pure V_3Sb_2 samples by varying the final sintering temperatures between 750 and 900 °C. After tries and errors, we eventually obtained two V_3Sb_2 polycrystalline samples with relatively high purity as examined by XRD. Hereafter, these two samples sintered at 780 °C and 830 °C are labeled as S1 and S2, respectively. Since their physical properties show some different behaviors, in the following we present the experimental results of both samples comparatively so as to

underline the fact that the physical properties of V_3Sb_2 are sensitive to the preparation conditions.

Figure 1 shows the XRD pattern of these two V_3Sb_2 samples after Rietveld refinement. It confirms that the obtained samples are nearly single phase with a small amount of impurity, which can be identified as V_3Sb for S1. The impurity phase is too weak to be identified for S2. The main phase of the XRD pattern can be refined by considering the hexagonal Fe_3Sn_2 -type structure model (space group $R\bar{3}m$, No. 166) with one V position at the 18h (x, y, z) and two Sb positions at 6c ($0, 0, z$), respectively. As illustrated in Fig.1, the refinements are converged well with reliable factors $R_p = 2.66\%$, $R_{exp} = 2.48\%$, and $\chi^2 = 2.28$ for S1, and $R_p = 2.98\%$, $R_{exp} = 2.26\%$, and $\chi^2 = 3.78$ for S2. According to the scaling factors, the amount of V_3Sb impurity in S1 was estimated to be ~ 1.2 wt%, which is consistent with the observed weak main peak of V_3Sb as shown by asterisk in Fig. 1(a). The obtained structural parameters for both samples are listed in Table I for comparison. As can be seen, the sample S1 has a shorter a but a longer c , leading to a slightly smaller V in comparison with those of sample S2. However, the differences are quite small, with the relative difference being smaller than 0.3%. These lattice parameters are also consistent with those reported in literature for LT- V_3Sb_2 [50]. In contrary, the positions of the atoms, especially along the z -axis, show a relatively large difference. Taking the V site as an example, the difference of the z -axis position is about 2.5% for these two samples, which result in a difference in the bond length along the c -axis as discussed below. However, it should be noted that synchrotron-based XRD is desirable to have more accurate determinations of the structural details.

The crystal structure of V_3Sb_2 is schematically shown in Fig. 2 by taking the refined structural information of S1. As seen in Fig. 2(a), the crystal structure of V_3Sb_2 is composed of Sb1 single layer and V-Sb2 bilayer that are stacked alternatively along the c -axis. The Sb1 atoms in the single layer form a 2D graphene-like honeycomb lattice, Fig.2(b), while the V-Sb2 bilayer consists of two V kagome layers with Sb2 atoms embedded in the center of the V hexagons, Fig. 2(c). For each V kagome layer, there are two kinds of equilateral triangles with different V-V bond lengths, i.e., 2.8600(19) Å and 2.6839(19) Å for S1 [2.864(4) Å and 2.691(4) Å for S2], as shown in purple and blue in Fig. 2(d). This means that the kagome lattice is not ideal, different from that in AV_3Sb_5 . As shown in Fig. 2(e), the V atoms of the smaller V triangles in two adjacent layers can be viewed to form a V_6 octahedra with an interlayer V-V distance of 2.773(4) Å for S1 [2.870(6) Å for S2]. For S1, this value is equal to the average of two intralayer nearest-neighbor V-V bond lengths. Such a small interlayer distance should produce a relatively strong interlayer interaction. However, the interlayer V-V bond length for S2 is found to be $\sim 3\%$ longer than the average of ab plane, which might result in weaker interlayer interactions.

Figure 3(a, b) shows the temperature-dependent magnetic susceptibility $\chi(T)$ of these two V_3Sb_2 samples measured in the temperature range 1.8-300 K under an external magnetic field of $\mu_0H = 1$ T. The experimental procedure is following: we first cooled the sample under zero field from room temperature to the lowest temperature, then applied 1 T field and recorded $\chi(T)$ upon heating up to room temperature, followed by

measuring $\chi(T)$ upon cooling down to the lowest temperature under 1 T. They are thus denoted as the ZFCw- and FCC- $\chi(T)$, respectively. As seen in Fig. 3(a), the ZFCw- and FCC- $\chi(T)$ curves of S1 exhibit a step-like anomaly around 160 K, below which the magnetic susceptibility is reduced. In addition, an obvious thermal hysteresis is evidenced around the transition, implying a first-order nature of this transition. The transition temperatures, T_{dw}^χ , defined from the maximum of $d\chi/dT$, are ~ 159 K and ~ 165 K for S1 in the cooling and heating processes, respectively, as shown in the top of Fig. 3(a). The $\chi(T)$ curves of S2 are basically similar to those of S1, but the transition is much wide and the thermal hysteresis becomes very weak, Fig. 3(b). In addition, the transition temperatures, $T_{dw}^\chi \approx 154$ K and 158 K for the cooling and heating processes, are lower than those of S1. These comparisons indicate that the quality of S1 is better than that of S2. We note that the observed feature in the magnetic susceptibility is very similar to those seen in some typical CDW materials, such as 1T-TaS₂ [58], NbSe₃ [59], CuIr₂Te₄ [60], IrTe₂ [61], and AV₃Sb₅ [12,36,47].

Except for the transition region, the ZFCw- and FCC- $\chi(T)$ curves are almost overlapped with each other in the whole temperature range, and show a paramagnetic behavior at high temperature and a low-temperature upturn without long-range magnetic order down to 1.8 K. As shown in Fig. 3(c), the inverse susceptibility $\chi^{-1}(T)$ of S1 in the low-temperature range 2-10 K can be fitted by a Curie-Weiss (CW) model, $\chi(T) = C/(T - \theta_{CW})$. Here, the obtained effective moment of $\mu_{\text{eff}} = 0.34 \mu_B/V$ and a CW temperature of $\theta_{CW} = -38.5$ K are similar with those of $0.22 \mu_B/V$ and -47.2 K in KV₃Sb₅ [36]. Noted that the $\chi^{-1}(T)$ in the high-temperature range 200-300 K seems to also follow a linear behavior, and a CW fitting yields $\mu_{\text{eff}} = 3.07 \mu_B/V$ and $\theta_{CW} = -4820$ K, respectively. Such a large θ_{CW} is not physically meaningful and is consistent with a Pauli paramagnetism.

Figure 3(d) presents the field dependence of magnetization $M(H)$ for S1 between -7 and +7 T at various temperatures. The $M(H)$ curves at all temperatures except for 1.8 K exhibit a linear dependence on the external field with no hysteresis, confirming the absence of ferromagnetic contributions to the magnetism. The magnetic moment of $\sim 0.003 \mu_B/V$ at 7 T is small. These results make it significantly different from Fe₃Sn₂, but similar with the AV₃Sb₅ family where no magnetic order or even local moment of V ion was found. In the isostructural compound Fe₃Sn₂, the Fe atoms in the kagome plane exhibit strong frustrated magnetic interactions, undergoing complex magnetic phase transitions upon cooling down from a paramagnetic to a collinear ferromagnetic state at 640 K, then to a non-collinear ferromagnetic state at 350 K, and finally to a re-entrant spin glass phase at 70 K [62]. In addition, we find that the magnitudes of $\chi(T)$ and $M(H)$ for V₃Sb₂ are very close to those of KV₃Sb₅ [36], further indicating the similarity of magnetic states in these two V-based kagome systems.

The presence of a density-wave-like transition in V₃Sb₂ is further confirmed by the resistivity measurement. Figure 4(a) shows the temperature-dependent $\rho(T)$ of S1 measured in a thermal cycle under 0 T. As can be seen, it displays a metallic behavior in the whole temperature range and exhibits a clear hump-like anomaly around $T_{dw}^\rho \approx 157$ K and 165 K in the cooling and heating processes. These transition temperatures defined from the dip of $d\rho/dT$ curve are in well agreement with those determined from

the $\chi(T)$ data shown in Fig. 3(a). In addition, a similar thermal hysteresis is evidenced around T_{dw} in $\rho(T)$. We find that the application of 10 T external magnetic field has a negligible influence on the $\rho(T)$ near T_{dw} (data not shown). This result indicates that the transition is most likely due to the formation of CDW order rather than SDW. A small positive magnetoresistance (MR) was evidenced at low temperatures. The inset of Fig. 4(a) displays the $\text{MR} \equiv \Delta\rho(H)/\rho(0) \times 100\%$ at 2 K in the field range from -14 T to 14 T. As can be seen, the MR is only $\sim 1.2\%$ at 2 K and 14 T, but it is non-saturating and can be well described by the expression $\text{MR} \propto H^n$ with $n = 1.35$.

Interestingly, the $\rho(T)$ of S2 is quite different with respect to that of S1 as seen in Fig. 4(b). Nonetheless, it also exhibits a pronounced anomaly centered around 150-160 K, and the transition temperatures determined from the minimum of $d\rho/dT$ are 152 K and 160 K in the cooling and heating processes, respectively. These temperatures are also consistent with those determined from the $\chi(T)$ data shown in Fig. 3(b). In comparison with S1, the transition is much stronger and extended over a wider temperature range. In addition, the resistivity below T_{dw} becomes higher than that above the transition and displays a clear upturn at low temperatures. These comparisons highlight a better quality of sample S1 than that of S2. These differences might be attributed to the fact the final sintering temperature of 830 °C for S2 is closer to the peritectoid temperature [50]. In the following we thus focus our attention on S1. Despite of these differences, the occurrence of density-wave-like transition, most likely a CDW one, around $T_{\text{dw}} \approx 160$ K in V_3Sb_2 should be an intrinsic and robust behavior.

To further characterize the paramagnetic and metallic ground state of V_3Sb_2 with a possible CDW-like transition, we performed specific-heat measurements on S1 in the wide temperature range. Figure 5 displays the C/T vs T of S1 from 2 to 250 K under zero field. There is no obvious specific-heat anomaly near the CDW-like transition, suggesting that the thermodynamic signature of this transition is too weak to be observed. The polycrystalline nature of the studied sample might also diminish the feature in specific heat, as occurred in the polycrystalline samples of AV_3Sb_5 ($A = \text{K}, \text{Rb}, \text{Cs}$) [12,36,47]. Inset of Fig. 5 shows the plot of C/T vs T^2 at the low-temperature range, and a linear fit to $C(T) = \gamma T + \beta T^3$ considering the electronic and lattice contributions yields the Sommerfeld coefficient $\gamma = 18.5(1) \text{ mJ mol}^{-1} \text{ K}^{-2}$ and $\beta = 0.73(1) \text{ mJ mol}^{-1} \text{ K}^{-4}$. The Debye temperature $\Theta_D \approx 237$ K can be calculated according to the relation $\Theta_D = (12\pi^4 nR/5\beta)^{1/3}$, where $R = 8.314 \text{ J mol}^{-1} \text{ K}^{-1}$ is the ideal gas constant and $n = 5$ is the number of atoms per formula unit. The obtained γ is relatively large compared with elemental metal and is very close to that of KV_3Sb_5 [36], implying the moderate enhancement of effective electron mass and the presence of electronic correlations.

From the above characterizations, we can conclude that the bilayer kagome metal V_3Sb_2 is a paramagnetic metal and undergoes a CDW-like transition at $T_{\text{dw}} \approx 160$ K, which is similar to the family of AV_3Sb_5 . But no superconductivity was observed in V_3Sb_2 at ambient pressure down to 1.8 K. To explore whether superconductivity emerges after suppressing the CDW under pressure, we measured the $\rho(T)$ of S1 under various hydrostatic pressures up to 1.8 GPa by using a piston-cylinder cell. The $\rho(T)$ and its

derivative $d\rho/dT$ at different pressures are shown in Fig. 6(a). The evolution of the CDW-like transition with pressure can be tracked clearly from the resistivity anomaly. With increasing pressure gradually, the anomaly in $\rho(T)$ and the corresponding T_{dw} determined from the minimum of $d\rho/dT$ continuously move to lower temperatures. The pressure dependence of the determined T_{dw} is plotted in Fig. 6(b). As can be seen, T_{dw} is suppressed to about 60 K at 1.6 GPa, above which it cannot be clearly distinguished in both $\rho(T)$ and $d\rho/dT$, implying a complete suppression of CDW-like order above 1.6 GPa. However, no sign of superconductivity can be observed down to 1.5 K near the putative quantum critical point of CDW-like order. Whether superconductivity can be realized at much lower temperatures or on high-quality single-crystal samples deserves further studies.

Finally, we calculated the electronic structure of $V_3\text{Sb}_2$ by first-principles calculations. As shown in Fig. 7, the $V_3\text{Sb}_2$ shows a metallic nature and its Fermi surface is mainly composed by V's d orbitals. In $V_3\text{Sb}_2$, there are two kinds of antimony, which are chemically inequivalent, forming different bands. The hybridization between Sb2 and V is relatively stronger than that between Sb1 and V, because Sb2 are intralayer with V atoms. Meanwhile, we calculated the topological indices of $V_3\text{Sb}_2$, which are $z_{2w,1}=0$, $z_{2w,2}=0$, $z_{2w,3}=0$ and $z_4=2$, showing a non-trivial topological crystalline property [55-57].

The present work is a preliminary study on the physical properties of $V_3\text{Sb}_2$ polycrystalline samples and leaves many open questions in the future study from both experimental and theoretical point of views. For example, electrical transport and magnetic properties at much lower temperatures should be measured to explore possible superconductivity or magnetic order. Variable-temperature XRD, transmission electron microscope, optical spectroscopy, and scanning tunneling microscope measurements should be performed to elucidate the nature of the density-wave-like transition. Moreover, to acquire high-quality single-crystal samples is mandatory for in-depth characterizations of the intrinsic electronic structure by using the angle-resolved photoemission spectroscopy.

Conclusion

In summary, we have synthesized the polycrystalline sample of $V_3\text{Sb}_2$ with bilayer kagome lattice of V atoms through a traditional solid-state-reaction method and characterized its structural, electrical transport, magnetic, and thermodynamic properties via x-ray powder diffraction, resistivity, magnetic susceptibility, and specific heat measurements. We observed no long-range magnetic order in $V_3\text{Sb}_2$ above 1.8 K, which is completely different from the isostructural Fe_3Sn_2 but similar to the kagome metal $AV_3\text{Sb}_5$ ($A = \text{K}, \text{Rb}, \text{Cs}$) family. In addition, a density-wave-like anomaly was evidenced around 160 K in $V_3\text{Sb}_2$, making it similar to the $AV_3\text{Sb}_5$ ($A = \text{K}, \text{Rb}, \text{Cs}$) family. Moreover, we find that the density-wave-like transition can be gradually suppressed by pressure but no sign of superconductivity can be observed down to 1.5 K near the putative quantum critical point. We proposed that $V_3\text{Sb}_2$ is a novel candidate

kagome metal to study the interplay between density-wave-order, nontrivial band topology and possible superconductivity.

Note added:

During the preparation of this manuscript, we noticed that Shi *et al.* reported the synthesis and characterizations of the “V₆Sb₄” single crystal in a recent preprint arXiv: 2110.09782 [63]. The “V₆Sb₄” single crystal was grown at a high temperature of 1100 °C and does not exhibit any density-wave-like transition, different from what we observed in the low-temperature phase of V₃Sb₂ in the present work. We attributed the observed different behaviors to the different sintering temperatures.

Acknowledgements

We acknowledge the useful discussions with Dr. Jiaqiang Yan. This work is supported by National Key R&D Program of China (2018YFA0305700, 2018YFA0305800), the National Natural Science Foundation of China (Grant Nos. 12025408, 11874400, 11834016, 11921004, 11888101, 11904391), the Beijing Natural Science Foundation (Z190008), the Strategic Priority Research Program and Key Research Program of Frontier Sciences of CAS (XDB25000000, XDB33000000 and QYZDB-SSW-SLH013), and the CAS Interdisciplinary Innovation Team (JCTD-201-01).

References

- [1] H. M. Guo and M. Franz, Topological insulator on the kagome lattice. *Phys. Rev. B* **80**, 113102 (2009).
- [2] L. Balents, Spin liquids in frustrated magnets. *Nature* **464**, 199 (2010).
- [3] S. Yan, D. A. Huse, and S. R. White, Spin-Liquid Ground State of the S=1/2 Kagome Heisenberg Antiferromagnet. *Science* **332**, 1173 (2011).
- [4] S. Depenbrock, I. P. McCulloch, and U. Schollwoeck, Nature of the Spin-Liquid Ground State of the S=1/2 Heisenberg Model on the Kagome Lattice. *Phys. Rev. Lett.* **109**, 067201 (2012).
- [5] T. H. Han, J. S. Helton, S. Chu, D. G. Nocera, J. A. Rodriguez-Rivera, C. Broholm, and Y. S. Lee, Fractionalized excitations in the spin-liquid state of a kagome-lattice antiferromagnet. *Nature* **492**, 406 (2012).
- [6] E. Liu, Y. Sun, N. Kumar, L. Muechler, A. Sun, L. Jiao, S. Y. Yang, D. Liu, A. Liang, Q. Xu, J. Kroder, V. Suess, H. Borrmann, C. Shekhar, Z. S. Wang, C. Y. Xi, W. H. Wang, W. Schnelle, S. Wirth, Y. Chen, S. T. B. Goennenwein, and C. Felser, Giant anomalous Hall effect in a ferromagnetic kagome-lattice semimetal. *Nat. Phys.* **14**, 1125 (2018).
- [7] L. Ye, M. Kang, J. W. Liu, F. von Cube, C. R. Wicker, T. Suzuki, C. Jozwiak, A. Bostwick, E. Rotenberg, D. C. Bell, L. Fu, R. Comin, and J. G. Checkelsky, Massive Dirac fermions in a ferromagnetic kagome metal. *Nature* **555**, 638 (2018).
- [8] J. X. Yin, S. S. Zhang, H. Li, K. Jiang, G. Q. Chang, B. J. Zhang, B. Lian, C. Xiang, I. Belopolski, H. Zheng, T. A. Cochran, S. Y. Xu, G. Bian, K. Liu, T. R. Chang, H. Lin, Z. Y. Lu, Z. Q. Wang, S. Jia, W. H. Wang, and M. Z. Hasan, Giant and anisotropic

- many-body spin-orbit tunability in a strongly correlated kagome magnet. *Nature* **562**, 91 (2018).
- [9] M. Kang, S. Fang, L. Ye, H. C. Po, J. Denlinger, C. Jozwiak, A. Bostwick, E. Rotenberg, E. Kaxiras, J. G. Checkelsky, and R. Comin, Topological flat bands in frustrated kagome lattice CoSn. *Nat. Commun.* **11**, 4004 (2020).
- [10] M. Kang, L. Ye, S. Fang, J.-S. You, A. Levitan, M. Han, J. I. Facio, C. Jozwiak, A. Bostwick, E. Rotenberg, M. K. Chan, R. D. McDonald, D. Graf, K. Kaznatcheev, E. Vescovo, D. C. Bell, E. Kaxiras, J. van den Brink, M. Richter, M. Prasad Ghimire, J. G. Checkelsky, and R. Comin, Dirac fermions and flat bands in the ideal kagome metal FeSn. *Nat. Mater.* **19**, 163 (2020).
- [11] Z. H. Liu, M. Li, Q. Wang, G. W. Wang, C. H. P. Wen, K. Jiang, X. L. Lu, S. C. Yan, Y. B. Huang, D. W. Shen, J. X. Yin, Z. Q. Wang, Z. P. Yin, H. C. Lei, and S. C. Wang, Orbital-selective Dirac fermions and extremely flat bands in frustrated kagome-lattice metal CoSn. *Nat. Commun.* **11**, 4002 (2020).
- [12] B. R. Ortiz, S. M. L. Teicher, Y. Hu, J. L. Zuo, P. M. Sarte, E. C. Schueller, A. M. M. Abeykoon, M. J. Krogstad, S. Rosenkranz, R. Osborn, R. Seshadri, L. Balents, J. He, and S. D. Wilson, CsV₃Sb₅: A Z₂ Topological Kagome Metal with a Superconducting Ground State. *Phys. Rev. Lett.* **125**, 247002 (2020).
- [13] J. X. Yin, W. L. Ma, T. A. Cochran, X. T. Xu, S. S. Zhang, H. J. Tien, N. Shumiya, G. M. Cheng, K. Jiang, B. Lian, Z. Song, G. Q. Chang, I. Belopolski, D. Multer, M. Litskevich, Z.-J. Cheng, X. P. Yang, B. Swidler, H. B. Zhou, H. Lin, T. Neupert, Z. Q. Wang, N. Yao, T.-R. Chang, S. Jia, and M. Zahid Hasan, Quantum-limit Chern topological magnetism in TbMn₆Sn₆. *Nature* **583**, 533 (2020).
- [14] M. P. Shores, E. A. Nytko, B. M. Bartlett, and D. G. Nocera, A Structurally Perfect S = 1/2 Kagomé Antiferromagnet. *J. Am. Chem. Soc.* **127**, 13462 (2005).
- [15] J. S. Helton, K. Matan, M. P. Shores, E. A. Nytko, B. M. Bartlett, Y. Yoshida, Y. Takano, A. Suslov, Y. Qiu, J. H. Chung, D. G. Nocera, and Y. S. Lee, Spin dynamics of the spin-1/2 Kagome lattice antiferromagnet ZnCu₃(OH)(6)Cl₂. *Phys. Rev. Lett.* **98**, 107204 (2007).
- [16] Y. Ran, M. Hermele, P. A. Lee, and X.-G. Wen, Projected-wave-function study of the spin-1/2 Heisenberg model on the kagome lattice. *Phys. Rev. Lett.* **98**, 117205 (2007).
- [17] M. Rigol and R. R. P. Singh, Magnetic susceptibility of the Kagome antiferromagnet ZnCu₃(OH)(6)Cl₂. *Phys. Rev. Lett.* **98**, 207204 (2007).
- [18] M. Punk, D. Chowdhury, and S. Sachdev, Topological excitations and the dynamic structure factor of spin liquids on the kagome lattice. *Nat. Phys.* **10**, 289 (2014).
- [19] Z. A. Kelly, M. J. Gallagher, and T. M. McQueen, Electron Doping a Kagome Spin Liquid. *Phys. Rev. X* **6**, 041007 (2016).
- [20] A. O'Brien, F. Pollmann, and P. Fulde, Strongly correlated fermions on a kagome lattice. *Phys. Rev. B* **81**, 235115 (2010).
- [21] S. L. Yu and J. X. Li, Chiral superconducting phase and chiral spin-density-wave phase in a Hubbard model on the kagome lattice. *Phys. Rev. B* **85**, 144402 (2012).
- [22] M. L. Kiesel, C. Platt, and R. Thomale, Unconventional Fermi Surface Instabilities in the Kagome Hubbard Model. *Phys. Rev. Lett.* **110**, 126405 (2013).

- [23] W. S. Wang, Z. Z. Li, Y. Y. Xiang, and Q. H. Wang, Competing electronic orders on kagome lattices at van Hove filling. *Phys. Rev. B* **87**, 115135 (2013).
- [24] I. I. Mazin, H. O. Jeschke, F. Lechermann, H. Lee, M. Fink, R. Thomale, and R. Valenti, Theoretical prediction of a strongly correlated Dirac metal. *Nat. Commun.* **5**, 4261 (2014).
- [25] S. V. Isakov, S. Wessel, R. G. Melko, K. Sengupta, and Y. B. Kim, Hard-core bosons on the kagome lattice: Valence-bond solids and their quantum melting. *Phys. Rev. Lett.* **97**, 147202 (2006).
- [26] S. Guertler, Kagome lattice Hubbard model at half filling. *Phys. Rev. B* **90**, 081105 (2014).
- [27] H. X. Li, T. T. Zhang, T. Yilmaz, Y. Y. Pai, C. E. Marvinney, A. Said, Q. W. Yin, C. S. Gong, Z. J. Tu, E. Vescovo, C. S. Nelson, R. G. Moore, S. Murakami, H. C. Lei, H. N. Lee, B. J. Lawrie, and H. Miao, Observation of Unconventional Charge Density Wave without Acoustic Phonon Anomaly in Kagome Superconductors AV_3Sb_5 ($A = Rb, Cs$). *Phys. Rev. X* **11**, 031050 (2021).
- [28] Z. X. Wang, Q. Wu, Q. W. Yin, C. S. Gong, Z. J. Tu, T. Lin, Q. M. Liu, L. Y. Shi, S. J. Zhang, D. Wu, H. C. Lei, T. Dong, and N. L. Wang, Unconventional charge density wave and photoinduced lattice symmetry change in the kagome metal CsV_3Sb_5 probed by time-resolved spectroscopy. *Phys. Rev. B* **104**, 165110 (2021).
- [29] F. H. Yu, D. H. Ma, W. Z. Zhuo, S. Q. Liu, X. K. Wen, B. Lei, J. J. Ying, and X. H. Chen, Unusual competition of superconductivity and charge-density-wave state in a compressed topological kagome metal. *Nat. Commun.* **12**, 3645 (2021).
- [30] W.-H. Ko, P. A. Lee, and X.-G. Wen, Doped kagome system as exotic superconductor. *Phys. Rev. B* **79**, 214502 (2009).
- [31] Q. Wang, S. S. Sun, X. Zhang, F. Pang, and H. C. Lei, Anomalous Hall effect in a ferromagnetic Fe_3Sn_2 single crystal with a geometrically frustrated Fe bilayer kagome lattice. *Phys. Rev. B* **94**, 075135 (2016).
- [32] Z. Y. Lin, J. H. Choi, Q. Zhang, W. Qin, S. Yi, P. D. Wang, L. Li, Y. F. Wang, H. Zhang, Z. Sun, L. M. Wei, S. B. Zhang, T. F. Guo, Q. Y. Lu, J. H. Cho, C. G. Zeng, and Z. Y. Zhang, Flatbands and Emergent Ferromagnetic Ordering in Fe_3Sn_2 Kagome Lattices. *Phys. Rev. Lett.* **121**, 096401 (2018).
- [33] Q. Wang, Y. F. Xu, R. Lou, Z. H. Liu, M. Li, Y. B. Huang, D. W. Shen, H. M. Weng, S. C. Wang, and H. C. Lei, Large intrinsic anomalous Hall effect in half-metallic ferromagnet $Co_3Sn_2S_2$ with magnetic Weyl fermions. *Nat. Commun.* **9**, 4212 (2018).
- [34] S. Nakatsuji, N. Kiyohara, and T. Higo, Large anomalous Hall effect in a non-collinear antiferromagnet at room temperature. *Nature* **527**, 212 (2015).
- [35] Z. Y. Lin, C. Z. Wang, P. D. Wang, S. Yi, L. Li, Q. Zhang, Y. Wang, Z. Y. Wang, H. Huang, Y. Sun, Y. B. Huang, D. W. Shen, D. L. Feng, Z. Sun, J.-H. Cho, C. G. Zeng, and Z. Y. Zhang, Dirac fermions in antiferromagnetic $FeSn$ kagome lattices with combined space inversion and time-reversal symmetry. *Phys. Rev. B* **102**, 155103 (2020).
- [36] B. R. Ortiz, L. C. Gomes, J. R. Morey, M. Winiarski, M. Bordelon, J. S. Mangum, L. W. H. Oswald, J. A. Rodriguez-Rivera, J. R. Neilson, S. D. Wilson, E. Ertekin, T. M. McQueen, and E. S. Toberer, New kagome prototype materials: discovery of KV_3Sb_5 ,

- RbV₃Sb₅, and CsV₃Sb₅. *Phys. Rev. Mater.* **3**, 094407 (2019).
- [37] S. Y. Yang, Y. J. Wang, B. R. Ortiz, D. Liu, J. Gayles, E. Derunova, R. Gonzalez-Hernandez, L. Smejkal, Y. L. Chen, S. S. P. Parkin, S. D. Wilson, E. S. Toberer, T. McQueen, and M. N. Ali, Giant, unconventional anomalous Hall effect in the metallic frustrated magnet candidate, KV₃Sb₅. *Sci. Adv.* **6**, eabb6003 (2020).
- [38] H. Chen, H. T. Yang, B. Hu, Z. Zhao, J. Yuan, Y. Q. Xing, G. J. Qian, Z. H. Huang, G. Li, Y. H. Ye, S. Ma, S. L. Ni, H. Zhang, Q. W. Yin, C. S. Gong, Z. J. Tu, H. C. Lei, H. X. Tan, S. Zhou, C. M. Shen, X. L. Dong, B. H. Yan, Z. Q. Wang, and H. J. Gao, Roton pair density wave in a strong-coupling kagome superconductor. *Nature*, <https://doi.org/10.1038/s41586> (2021).
- [39] K. Y. Chen, N. N. Wang, Q. W. Yin, Y. H. Gu, K. Jiang, Z. J. Tu, C. S. Gong, Y. Uwatoko, J. P. Sun, H. C. Lei, J. P. Hu, and J. G. Cheng, Double Superconducting Dome and Triple Enhancement of T_c in the Kagome Superconductor CsV₃Sb₅ under High Pressure. *Phys. Rev. Lett.* **126**, 247001 (2021).
- [40] F. Du, S. S. Luo, B. R. Ortiz, Y. Chen, W. Y. Duan, D. T. Zhang, X. Lu, S. D. Wilson, Y. Song, and H. Q. Yuan, Pressure-induced double superconducting domes and charge instability in the kagome metal KV₃Sb₅. *Phys. Rev. B* **103**, L220504 (2021).
- [41] Y. X. Jiang, J. X. Yin, M. M. Denner, N. Shumiya, B. R. Ortiz, G. Xu, Z. Guguchia, J. He, M. S. Hossain, X. X. Liu, J. Ruff, L. Kautzsch, S. S. Zhang, G. Chang, I. Belopolski, Q. Zhang, T. A. Cochran, D. Multer, M. Litskevich, Z. J. Cheng, X. P. Yang, Z. Q. Wang, R. Thomale, T. Neupert, S. D. Wilson, and M. Z. Hasan, Unconventional chiral charge order in kagome superconductor KV₃Sb₅. *Nat. Mater.* **20**, 1353 (2021).
- [42] E. M. Kenney, B. R. Ortiz, C. Wang, S. D. Wilson, and M. J. Graf, Absence of local moments in the kagome metal KV₃Sb₅ as determined by muon spin spectroscopy. *J. Phys.: Condens. Matter* **33**, 235801 (2021).
- [43] Z. W. Liang, X. Y. Hou, F. Zhang, W. R. Ma, P. Wu, Z. Y. Zhang, F. H. Yu, J. J. Ying, K. Jiang, L. Shan, Z. Y. Wang, and X. H. Chen, Three-Dimensional Charge Density Wave and Surface Dependent Vortex Core States in a Kagome Superconductor CsV₃Sb₅. *Phys. Rev. X* **11**, 031026 (2021).
- [44] B. R. Ortiz, P. M. Sarte, E. M. Kenney, M. J. Graf, S. M. L. Teicher, R. Seshadri, and S. D. Wilson, Superconductivity in the Z₂ kagome metal KV₃Sb₅. *Phys. Rev. Mater.* **5**, 034801 (2021).
- [45] N. Shumiya, M. S. Hossain, J. X. Yin, Y. X. Jiang, B. R. Ortiz, H. X. Liu, Y. G. Shi, Q. W. Yin, H. C. Le, S. S. Zhan, G. Q. Chang, Q. Zhang, T. A. Cochran, D. Multer, M. Litskevich, Z. J. Cheng, X. P. Yang, Z. Guguchia, S. D. Wilson, and M. Z. Hasan, Intrinsic nature of chiral charge order in the kagome superconductor RbV₃Sb₅. *Phys. Rev. B* **104**, 035131 (2021).
- [46] Q. Wang, P. F. Kong, W. J. Shi, C. Y. Pei, C. H. P. Wen, L. L. Gao, Y. Zhao, Q. W. Yin, Y. S. Wu, G. Li, H. C. Lei, J. Li, Y. L. Chen, S. C. Yan, and Y. P. Qi, Charge Density Wave Orders and Enhanced Superconductivity under Pressure in the Kagome Metal CsV₃Sb₅. *Adv. Mater.* **33**, 2102813 (2021).
- [47] Q. W. Yin, Z. J. Tu, C. S. Gong, Y. Fu, S. H. Yan, and H. C. Lei, Superconductivity and Normal-State Properties of Kagome Metal RbV₃Sb₅ Single Crystals. *Chin. Phys. Lett.* **38**, 037403 (2021).

- [48]F. H. Yu, T. Wu, Z. Y. Wang, B. Lei, W. Z. Zhuo, J. J. Ying, and X. H. Chen, Concurrence of anomalous Hall effect and charge density wave in a superconducting topological kagome metal. *Phys. Rev. B* **104**, L041103 (2021).
- [49]H. Zhao, H. Li, B. R. Ortiz, S. M. L. Teicher, T. Park, M. X. Ye, Z. Q. Wang, L. Balents, S. D. Wilson, and I. Zeljkovic, Cascade of correlated electron states in a kagome superconductor CsV_3Sb_5 . *Nature*, <https://doi.org/10.1038/s41586> (2021).
- [50]F. Failamani, P. Broz, D. Macciò, S. Puchegger, H. Müller, L. Salamakha, H. Michor, A. Grytsiv, A. Saccone, E. Bauer, G. Giester, and P. Rogl, Constitution of the systems $\{\text{V,Nb,Ta}\}\text{-Sb}$ and physical properties of di-antimonides $\{\text{V,Nb,Ta}\}\text{Sb}_2$. *Intermetallics* **65**, 94 (2015).
- [51]Y. Uwatoko, S. Todo, K. Ueda, A. Uchida, M. Kosaka, N. Mori, and T. Matsumoto, Material properties of Ni-Cr-Al alloy and design of a 4 GPa class non-magnetic high-pressure cell. *J. Phys.: Condens. Matter* **14**, 11291 (2002).
- [52]G. Kresse and J. Furthmüller, Efficiency of ab-initio total energy calculations for metals and semiconductors using a plane-wave basis set. *Comp. Mater. Sci.* **6**, 15 (1996).
- [53]G. Kresse and D. Joubert, From ultrasoft pseudopotentials to the projector augmented-wave method. *Phys. Rev. B* **59**, 1758 (1999).
- [54]J. P. Perdew, K. Burke, and M. Ernzerhof, Generalized gradient approximation made simple (vol 77, pg 3865, 1996). *Phys. Rev. Lett.* **78**, 1396 (1997).
- [55]L. Fu, Topological Crystalline Insulators. *Phys. Rev. Lett.* **106**, 106802 (2011).
- [56]M. G. Vergniory, L. Elcoro, C. Felser, N. Regnault, B. A. Bernevig, and Z. Wang, A complete catalogue of high-quality topological materials. *Nature* **566**, 480 (2019).
- [57]Maia G. Vergniory, Benjamin J. Wieder, Luis Elcoro, Stuart S.P. Parkin, Claudia Felser, B. Andrei Bernevig, and N. Regnault, "All Topological Bands of All Stoichiometric Materials" (arXiv preprint (2021). arXiv:2105.09954.).
- [58]F. J. Disalvo and J. V. Waszczak, Paramagnetic Moments and Localization in 1T-TaS₂. *Phys. Rev. B* **22**, 4241 (1980).
- [59]F. J. Disalvo and J. V. Waszczak, Magnetic-susceptibility of NbSe₃ and TaSe₃. *J. Phys. Chem. Solids* **41**, 1311 (1980).
- [60]M. Boubeche, J. Yu, L. Chushan, W. Huichao, L. Y. Zeng, Y. He, X. P. Wang, W. Z. Su, M. Wang, D. X. Yao, Z. Wang, Jun, and H. X. Luo, Superconductivity and Charge Density Wave in Iodine-Doped CuIr_2Te_4 . *Chin. Phys. Lett.* **38**, 037401 (2021).
- [61]J. J. Yang, Y. J. Choi, Y. S. Oh, A. Hogan, Y. Horibe, K. Kim, B. I. Min, and S. W. Cheong, Charge-Orbital Density Wave and Superconductivity in the Strong Spin-Orbit Coupled $\text{IrTe}_2\text{:Pd}$. *Phys. Rev. Lett.* **108**, 116402 (2012).
- [62]D. Boldrin and A. S. Wills, Anomalous Hall Effect in Geometrically Frustrated Magnets. *Adv. Cond. Matter. Phys.* **2012**, 615295 (2012).
- [63]M. Z. Shi, F. H. Yu, Y. Yang, F. B. Meng, B. Lei, Y. Luo, Z. Sun, J. F. He, R. Wang, T. Wu, Z. Y. Wang, Z. J. Xiang, J. J. Ying, and X. H. Chen, A new class of bilayer kagome lattice compounds with Dirac nodal lines and pressure-induced superconductivity. arXiv:2110.09782 (2021).

Table 1. Lattice parameters, atomic coordinates, and isotropic thermal factors B_{iso} for V_3Sb_2 samples from powder XRD data at 295K.

	S1 (780 °C)	S2 (830 °C)
Space group, Z	$R\bar{3}m, Z = 6$	
a (Å)	5.5440(1)	5.5545(1)
c (Å)	20.3529(4)	20.3374(6)
V (Å ³)	541.76 (2)	543.40 (2)
V_x	0.49470(15)	0.49480(25)
V_y	0.50530(11)	0.50520(25)
V_z	0.11018(11)	0.10734(15)
B_{iso_V} (Å ²)	2.65(5)	2.32(3)
Sb1_z	0.33189(4)	0.33281(5)
$B_{\text{iso}_\text{Sb1}}$ (Å ²)	2.72(3)	2.41(3)
Sb2_z	0.11101(06)	0.10908(08)
$B_{\text{iso}_\text{Sb2}}$ (Å ²)	3.49(4)	2.76(5)
R_p (%)	2.66	2.98
R_{exp} (%)	2.48	2.26
χ^2	2.28	3.78
R_{Bragg} (%)	4.35	4.20

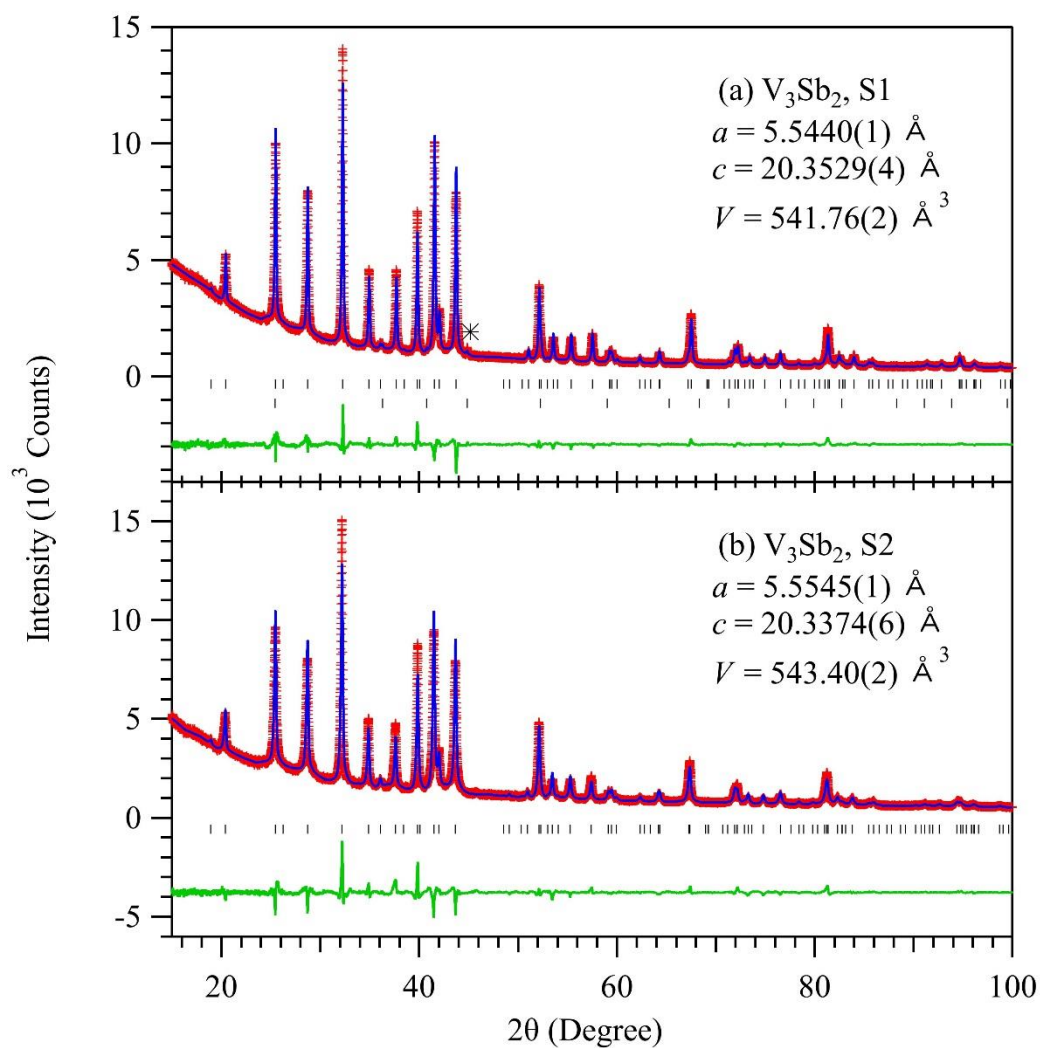


Figure 1. Observed (cross), calculated (solid line), and difference (bottom line) XRD profiles of the polycrystalline V_3Sb_2 samples: (a) S1 and (b) S2 after Rietveld refinements. Bragg positions of the main phase V_3Sb_2 and the impurity phase V_3Sb are indicated by the two rows of tick marks in (a), while only the position of V_3Sb_2 is shown in (b). The main peak of the V_3Sb impurity phase is marked by an asterisk in (a). The obtained lattice parameters for both samples are also given in the figure.

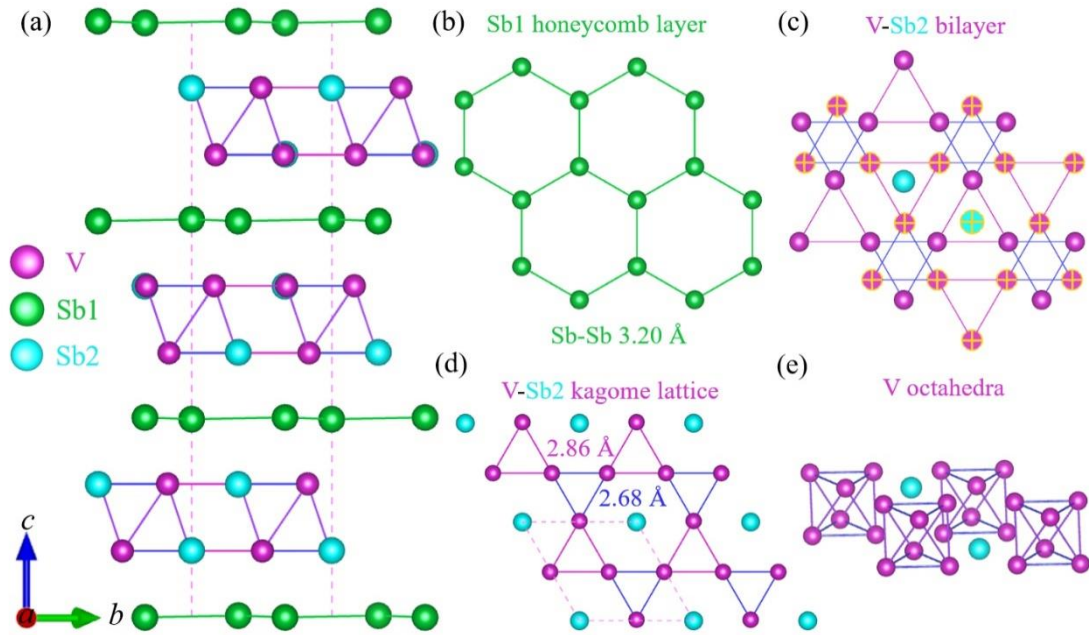


Figure 2. (a) A schematic view of the layered structure of V_3Sb_2 (side view) stacked by $Sb1$ and $V-Sb2$ layers along the c -axis. The unit cell is enclosed by the dashed lines. (b) The $Sb1$ atoms form a honeycomb sublattice below and above each $V-Sb2$ bilayer with $Sb1-Sb1$ bond length of 3.20 \AA . (c) The structure of the $V-Sb2$ layer. The V atoms form bilayer kagome lattice and the $Sb2$ atoms sit in the centers of V hexagons in each V kagome layer. (d) Single $V-Sb2$ kagome layer made of two kinds of equilateral triangles with the side length of 2.8602 \AA and 2.6839 \AA , shown in purple and blue, respectively. (e) The V triangles with smaller length (blue) in two layers form the V_6 octahedra. The bond-length values are taken from the refined results of the S1 sample

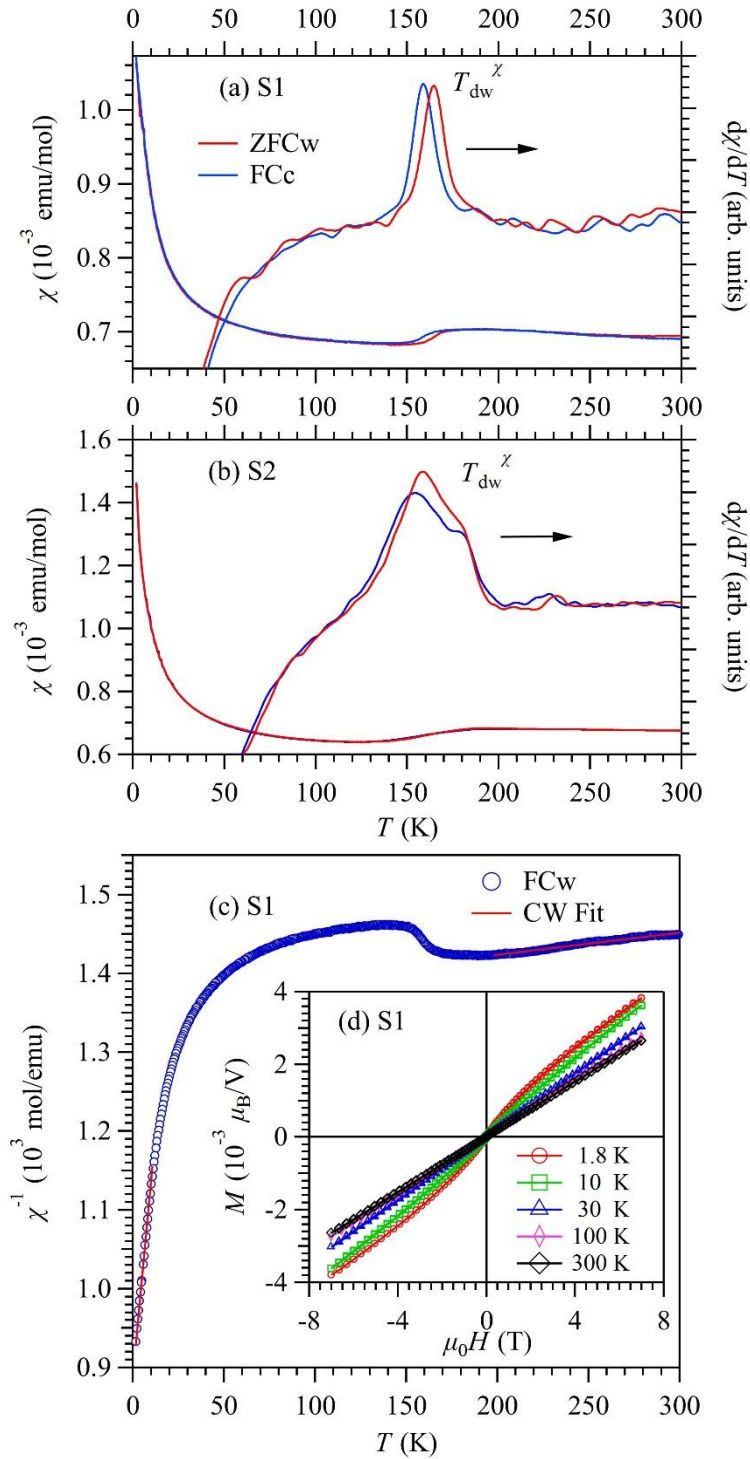


Figure 3. Temperature dependence of the dc magnetic susceptibility $\chi(T)$ and its derivative $d\chi/dT$ for V_3Sb_2 samples: (a) S1 and (b) S2, measured in the ZFCw and FCc modes under an external magnetic field of 1 T. The transition temperature T_{dw}^χ was defined as the peak of the $d\chi/dT$. (c) Temperature dependence of the inverse susceptibility $\chi^{-1}(T)$ for sample S1. The Curie-Weiss (CW) fitting curves are shown by the solid line in (c). (d) The isothermal magnetization $M(H)$ curves for sample S1 measured between +7 and -7 T at various temperatures.

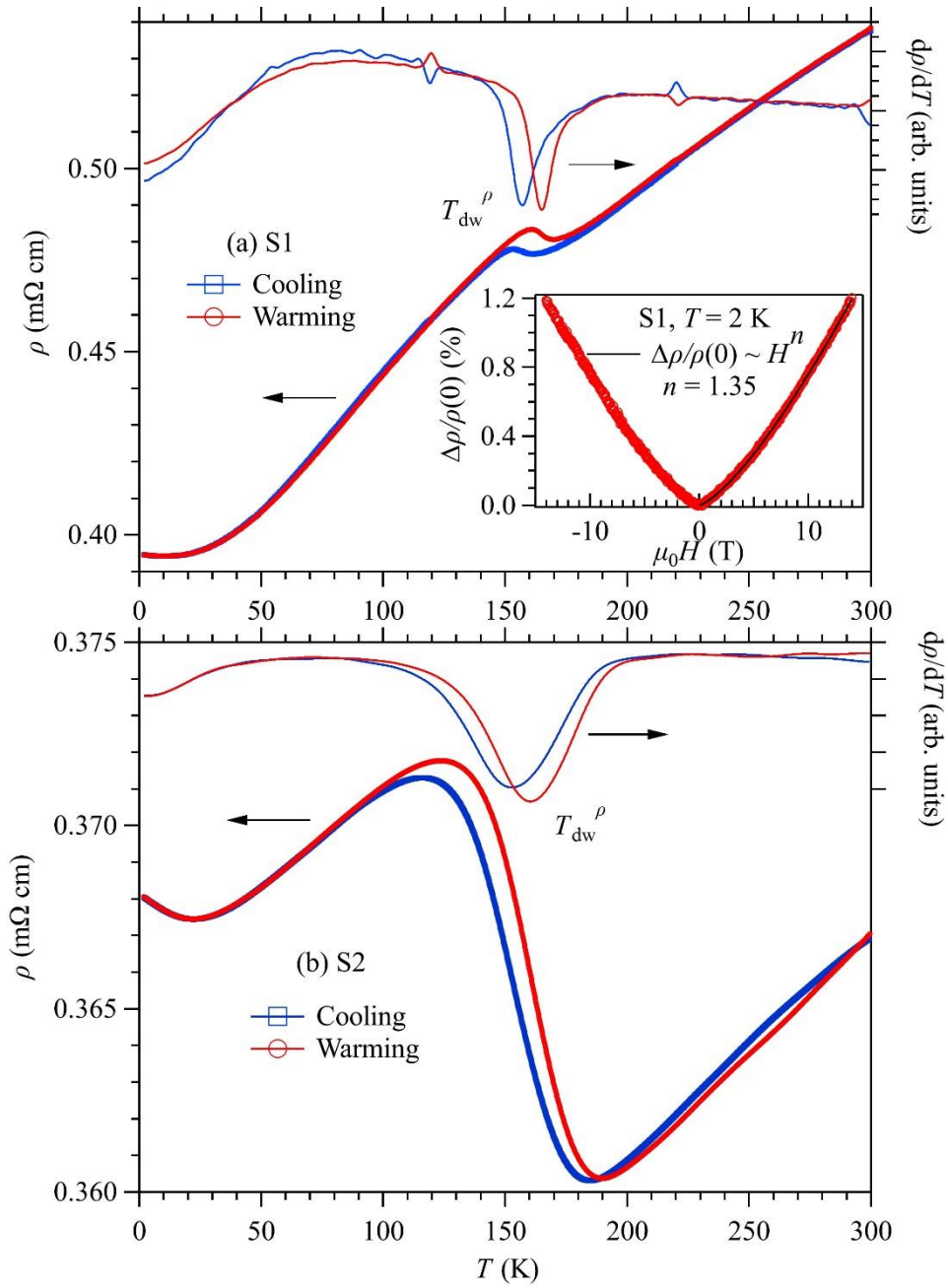


Figure 4. Temperature dependence of the resistivity $\rho(T)$ and its derivative $d\rho/dT$ for the V_3Sb_2 samples: (a) S1, (b) S2, measured in a thermal cycle under 0 T. The transition temperature T_{dw}^ρ was determined from the dip of $d\rho/dT$. Inset of (a) shows the magnetoresistance of S1 at 2 K under fields up to 14 T.

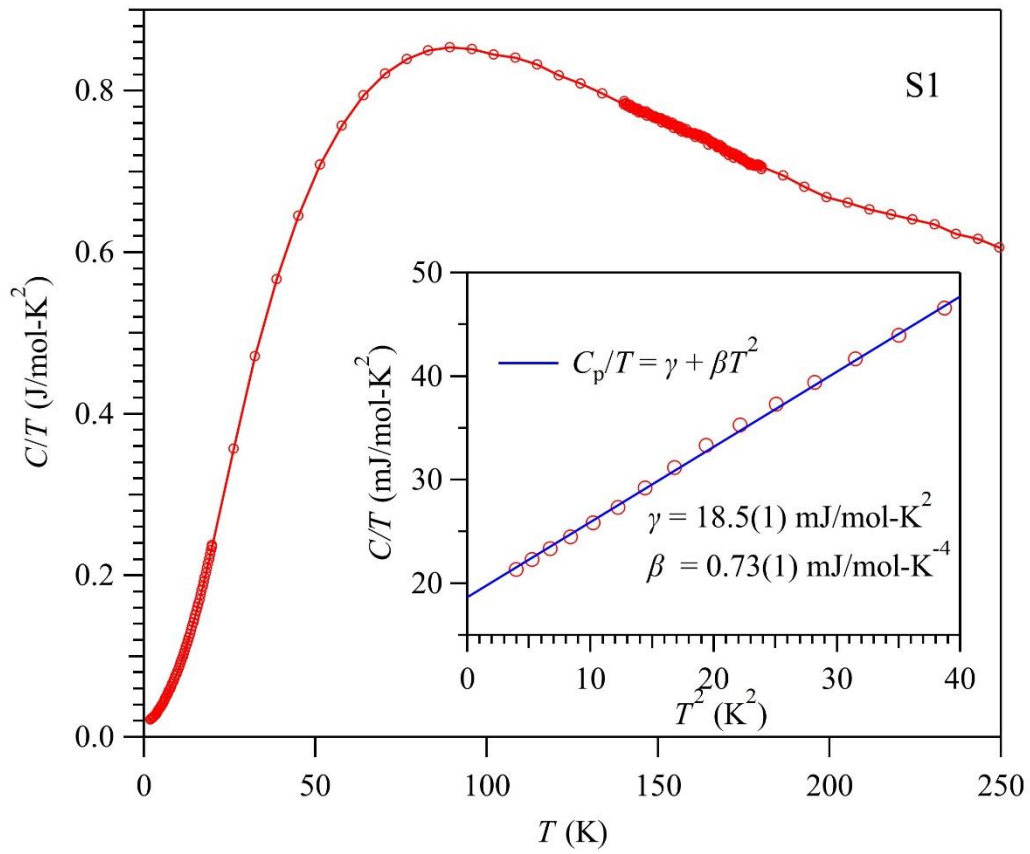


Figure 5. C/T vs T for V_3Sb_2 sample S1 in the wide temperature range from 2 to 250 K under zero field. Inset shows the C/T vs T^2 at the low-temperature range, which can be described by a sum of electronic and phonon contributions.

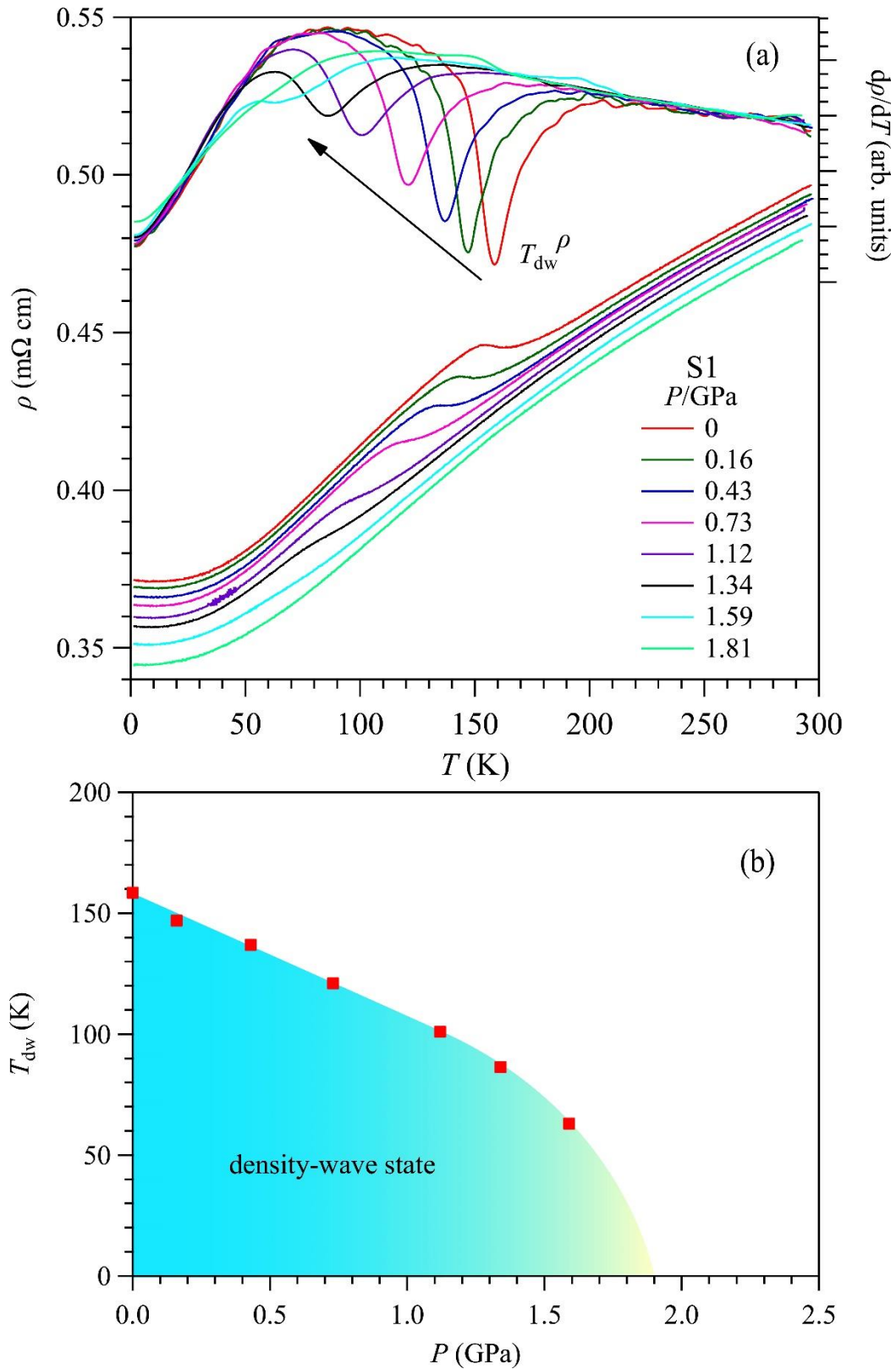


Figure 6. (a) Temperature dependence of the resistivity $\rho(T)$ and its derivative $d\rho/dT$ for the V₃Sb₂ sample S1 under various pressures up to 1.81 GPa measured with a piston-cylinder cell. (b) Pressure dependence of the density-wave-like transition temperature T_{dw} .

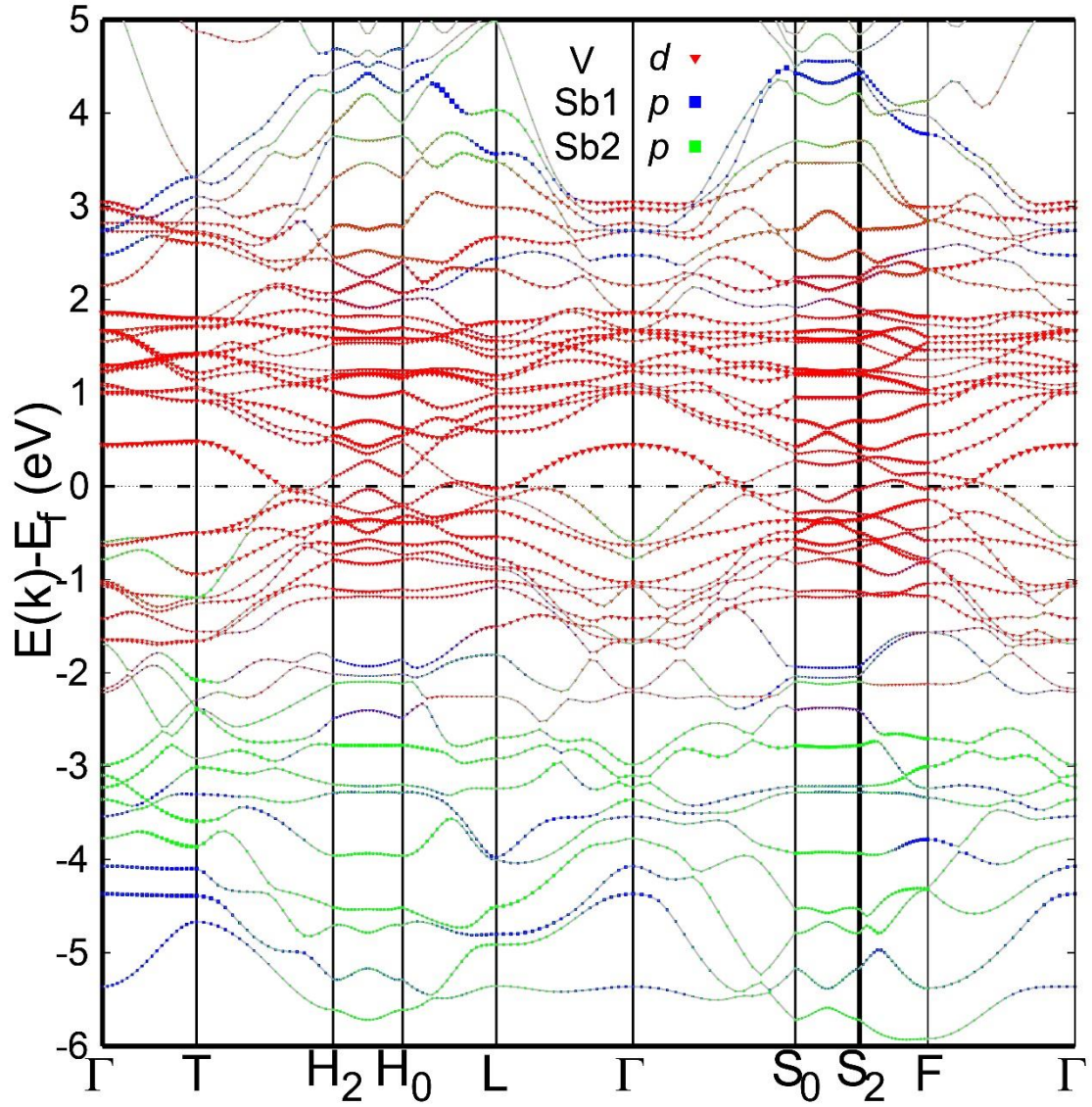


Figure 7. The projected band structures obtained from DFT calculations for V_3Sb_2 . The orbital characters of bands are represented by different colors and the projected weights are represented by the sizes.